

# Data-efficient, multi-objective machine learning approach for additively manufactured cellular materials

**Ye Wei<sup>1</sup>**

WEIYE@MAILS.Tsinghua.EDU.CN

**Yu Qin<sup>2</sup>**

QIN-Y17@MAILS.Tsinghua.EDU.CN

**Bo Peng<sup>2</sup>**

PENGBO21@MAILS.Tsinghua.EDU.CN

**Jiabao Dai<sup>2</sup>**

DJB18@MAILS.Tsinghua.EDU.CN

**Yue Li<sup>3</sup>**

L.HAN@MPIE.DE

**LiuLiu Han<sup>3</sup>**

YUE.LI@MPIE.DE

**Peng Wen<sup>2</sup>**

WENPENG@TSINGHUA.EDU.CN

<sup>1</sup>*Institute for Interdisciplinary Information Science, Tsinghua University, Peking, China*

<sup>2</sup>*Department of Mechanical Engineering, Tsinghua University, Peking, China*

<sup>3</sup>*Max Planck Institute für Eisenforschung GmbH, Düsseldorf, Germany*

**Editor:**

## Abstract

Cellular materials are among the most widely adopted engineering materials due to their high mechanical performance and adaptable properties. However, the design of such architected materials still generally relies on experts' prior knowledge and intuition. Here, we present an active learning approach to accelerate the multi-objective cellular materials design with a sparse dataset. We demonstrate our approach in the additively manufactured cellular scaffolds for orthopedic implants, which require the customized elastic modulus, high yield strength and fewer weights. Without any prior knowledge, our method efficiently discovered several light-weight scaffold architectures with proper elastic modulus and superior yield strength, thus providing a new route towards the accelerated discovery of the complex cellular materials.

**Keywords:** Cellular scaffolds; Bone fixation; Generative model; 3D Convolutional neural network; Finite element method; Additive manufacturing

## 1. Introduction

Consisting of solid and void networks, cellular materials can demonstrate a much broader range of physical properties than their constituent materials, achieving high mechanical efficiency with less energy consumption and less material wastage. Thus, cellular materials enjoy high popularity in many fields, such as light-weight structuresZheng et al. (2014); Jang et al. (2013); Meza et al. (2014); Li and Gao (2016); Kadic et al. (2012); Yang et al. (2022), acousticsLi et al. (2009), battery electrodesSchaedler et al. (2011) and electromagneticsSchurig et al. (2006); Magnus et al. (2008). Moreover, recent progress in additive manufacturing (AM) has further enabled the customized design and large-scale fabrication of complex cellular structures. Despite the broad applicability and immense potential of cellular materials, designing them is particularly challenging. Traditional cellular materials design approaches generally rely on numerical simulation, theoretical analysis, and topology optimization. These approaches usually require long and intense efforts of domain experts, and the performance of resultant designs highly depends on the designer's domain knowledge

and their initial guesses Christensen et al. (2015); Valdevit et al. (2011); Martin P. B (2003); Wang et al. (2014). Recently, Artificial intelligence (AI) has risen as a promising technique to circumvent this problem without requiring any prior knowledge Hanakata et al. (2018); Mao et al. (2020). However, current AI methods demand massive simulation data, and the datasets mainly consist of 2-dimensional cellular patterns. Moreover, real-world applications usually require multi-objective property optimization under several physical constraints [], yet the current AI methods work only for unconstrained single-objective optimization. Here, we propose a machine learning approach for data-efficient, multi-objective cellular scaffold design. More specifically, our framework aims at optimizing the yield strength and elastic modulus of the cellular scaffold simultaneously under the constraint of weight limitation. It consists of three main parts: 1) Targeted scaffold generation and selection. 2) Multi-objective active learning loop. 3) Additive manufacturing and testing.

As shown in Fig. 1, the first step is the Targeted Scaffold Generation (TSG). This step generates the initial set of scaffolds with unknown properties. In the second step, a Multi-objective Active Learning Loop ((MALL) and finite element analysis evaluate this set and search for the high-performance cellular structures iteratively. Active learning is a specialized machine learning algorithm which interactively queries an information source such that the algorithm identifies the high-value data with fewer labelled data than typical machine learning Rubens et al. (2015); Das et al. (2016). Such date efficiency is highly desirable since constructing a large dataset with known properties is very difficult both computationally and experimentally Rao et al. (2022). Finally, we fabricate the AI-designed scaffolds via specialized AM technique and perform the mechanical tests to verify the corresponding mechanical properties experimentally. Finally, we verify the mechanical properties of ML design via experimental compression testing. Altogether, we coined our method as the 'TSG-MALL'.

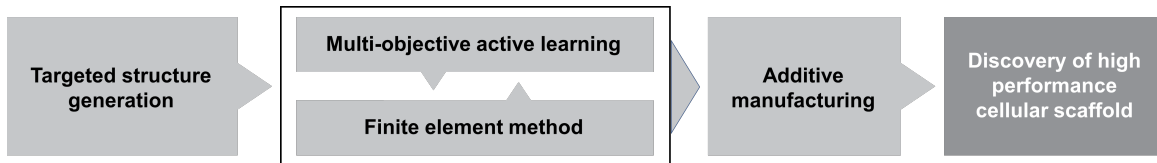


Figure 1: The overview of the active learning (TSG-MALL) workflow.

### 1.1 Machine learning algorithms

We applied the TSG-MALL approach to a multi-objective optimization problem with clinical importance - bone fixation, bone filling and joint replacement. The bone defect is a prevalent clinical problem, and metal cellular scaffolds are widely used for bone fixation and replacement. The current design of the cellular structure is a labor-intensive manual process, due to the patient-specific clinical requirements. Namely, the elastic modulus of human bones ranges from 0.03 to 30 GPa (Wang et al., 2016), whereas the existing metal scaffold's elastic modulus range from 0 to 140 GPa (Yang et al., 2020). The replacement scaffolds' elastic modulus must match that of the bones. Otherwise, the non-matched elastic modulus will lead to the stress shielding effect in the early stage of implantation (Yang et al., 2020). Meanwhile, The yield strength must be as high as possible to sustain the bone movement, whilst the weight shall not exceed certain limitations (Yang et al., 2020).

The cellular scaffold and its 3D-printed experimental counterpart are shown in inlets of Fig. 2 (a). It is a  $3 \times 3 \times 3$  cubic arrangement of the Gyroid unit. The Gyroid geometry belongs to the

triply periodic minimal surfaces (TPMS) family, which is an ideal structure for bone replacement due to its flexibility for property adjustment(Bidan et al., 2013; Downing et al., 2021). The TSG-MALL adjusts the mechanical properties of the scaffold by controlling the individual porosity. Fig. 2(b) shows the architectures of the 3D convolutional neural network (3D-CNN) for the E and Y prediction. The 3D-CNN is designated for the volumetric data representation learning (Krizhevsky et al., 2017; Alzubaidi et al., 2021). It contains three main components: the input, convolution, and output layers. At the input layer, the cellular scaffold is discretized into  $60 * 60 * 60$  pixels as input. Such discretization retains more geometrical information than porosity matrix input, resulting in less learning error. A pixel can be in either solid (1) or void (0) phase, corresponding to the solid or void part in the scaffold, respectively. The convolution layers consist of a series of 3D convolution kernels that extract high-level information about the input, and the output layer provides the final prediction. The dataset preparation protocol is described in Appendix. Fig. 2 (c) shows the 3D convolutional autoencoder (3D-CAE) with typical two-neural network architecture, an encoder and a decoder. 3D-CAE learns an efficient and effective representation of the high-dimension data in an unsupervised manner, which converts the search in high dimension design space to a lower one. It is noteworthy that the actual Gyroid structure is not used here because the decoder cannot reliably recover the original Gyroid geometry due to the non-zero reconstruction error. We circumvent this problem by adopting its corresponding porosity matrix, since it is a matrix that only contains positive scalars. The encoder  $q_\phi(z|x)$  with parameters  $\phi$  compresses the porosity matrix into a hidden feature representation using a neural encoder architecture. Then the decoder  $q_\theta(x|z)$  with parameters  $\theta$  reconstructs the output from such representation using a neural decoder. Hence, it learns the 'design principle' of the cellular scaffold from an unlabeled dataset (details in Appendix).

Fig. 2 (d) shows the primary step of the MALL workflow. The tasks are multi-objective: The designated scaffolds need to achieve specific  $E_{target}$ ; Y and porosity need to be as high as possible. This task can be mathematically formulated as:

Find  $x \in H$

To the mapping  $f: H \rightarrow Y$  and  $g: H \rightarrow E$

Such that  $x = argmax_{x \in H}(f(x))$  and  $g(x) = E_{target}$

Under the constraint: porosity  $\geq$  fixed constant

$H$  is the scaffold design space;  $f$  and  $g$  are the mappings of scaffold design to its corresponding  $Y$  and  $E$ . Firstly, the targeted generation is formulated as a process of sampling from the latent feature representation. Using Gaussian mixture modelling (GMM), we model the latent representation as a continuous probabilistic distribution. The following task is to sample the best scaffold candidates. The decoder processes the sampled high dimensional points to recover their original shape in real space, from which the  $E$  and  $Y$  are inferred by 3D-CNNs. The candidate selection method is a variant of epsilon-greedy search: each sampling iteration, we sample 2000 data points and select the candidates whose predicted  $E$  falls within the target range and yield strength goes higher than the best data point in the current dataset, with epsilon (5%) chances that we choose the lower ones. Finally, the selected data points will still be rejected if their mean porosity is 10 % higher than pre-set criteria. Such search method generally has a higher success rate than the Edisonian approach, which hinges on trial-and-error search(Russell and Norvig, 2016). Lastly, FEM calculates the  $E$  and  $Y$  of the queried scaffolds. The results will be returned to the training database, and the 3D-CNNs

will be re-trained for the next active learning iteration. MALL stops when all pre-set criteria are met.

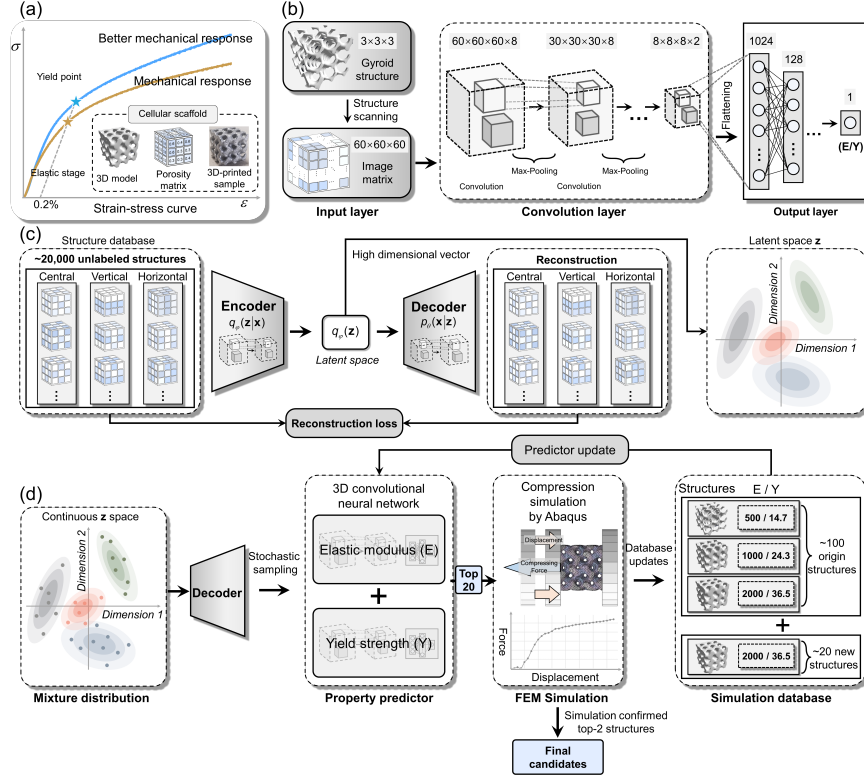


**Figure 2: The architecture of multi-objective active learning.** (a) The cellular scaffold in this study. The task is to improve the yield strength while fixating the Elastic modulus under the constraint of weight limitation. (b) The 3D-CNN architecture for predicting the elastic modulus and yield strength. (c) The generative model for targeted scaffold generation (d) The multi-objective active learning loop for the high-performance scaffold discovery.

## 1.2 Applications to orthopedic implants

According to the therapeutic needs, orthopedic metal materials are divided into non-degradable implants represented by titanium-based metals and degradable implants represented by zinc-based metals (Qin et al., 2022a,b). In this study, We illustrate the effectiveness of TSG-MALL with the Zinc materials. Fig. 3 shows the original data's E-Y distribution (marked by dark gray) with each active learning iteration characterized by colored regions. The task is to design high-Y cellular scaffolds at E=500 MPa and 1000 MPa (E500 and E1000). It is worth noting that the initial data does not contain any E500 and E1000 data points. Hence, TSG-MALL has to design E-specific Y-optimized scaffolds 'from scratch'. The uniform scaffolds at E = 500 and 1000 set the 'golden criteria' for the scaffolds' performance. TSG-MALL stops if the designed Y exceeds the 'golden criteria'. Table 2 demonstrates the average E, Y and porosity at each learning iteration (Appendix). For the E500 task, the first iteration scaffolds already contain some scaffolds with E≈500 Mpa, albeit the overall E distribution shows a significant standard deviation (Fig. 3 (b)). The second

iteration shows some improvement - the overall standard deviation is significantly reduced (from 52 to 19). While all scaffolds' E locate around 500 MPa, yield strength is still 30% less than the golden criteria. Gradual improvement ensued till the fifth iteration. The best candidate (15.2) is slightly better than the golden criteria (14.8). On the other hand, the TSG-MALL algorithm excels at E1000 tasks, outperforming the golden criteria by a large margin. The first iteration already shows excellent results. All designed scaffolds exhibit targeted E, with slightly worse Y ( $\approx 10\%$ ). The second iteration witnessed a significant decrease in porosity (from 0.41 to 0.34), which in turn enhanced yield strength remarkably. However, this strategy brings in another problem - the E increases to 1297 MPa and mean porosity also reduces by 15% (that means more than 15% increase in weight). TSG-MALL improved on this quickly and discovered the E-specific high-Y cellular scaffolds with proper porosity in the subsequent two iterations.

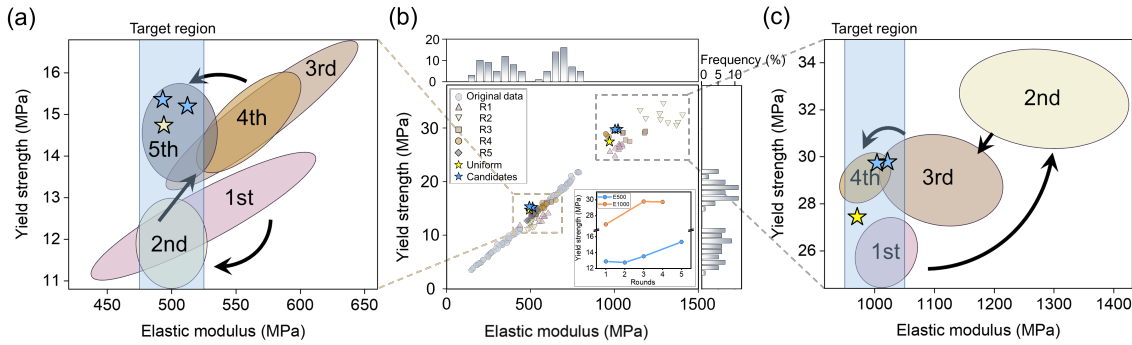


**Figure 3: The active learning process.** The colored regions indicate the area covered by active learning data and the learning path is indicated by black arrows. (a) E500 task. (b) Original and active learning data. (c) E1000 task.

Finally, the TSG-MALL-designed scaffolds were manufactured, and their relevant properties were measured experimentally (Table 1). As expected, A1 and A2 did not show any advantage over the uniform scaffold (U1). On the other hand, the B1 scaffold demonstrates a great advantage over the uniform U2 scaffold, whose  $Y$  ( $27.07 \pm 0.76$ ) exceeds the golden criteria ( $21.36 \pm 1.79$ ) by a large margin of 26.5%, with slightly lower porosity. To understand the AI-designed scaffolds, we further analyze the B1 scaffold by extracting the corresponding regression activation map (RAM) and performing the FEM mechanical analysis. Specifically, we apply the RAM to the Y-predicting 3D-CNN to interpret the driving mechanism behind the high yield strength. RAM is a variant of a classification activation map, which extracts the last convolutional layer to visualize the discriminative regions used by the 3D-CNN to predict the output (Meng et al., 2019). In this case, RAM highlights the scaffold's spatial characteristics that correlate to its mechanical properties, thus shedding light on the design principle of the cellular scaffold. Fig. 4(f) demonstrates the x-z axis cross-section of RAM of B1 and U2 scaffolds. RAM shows that the 'attention' of CNN on the B1 scaffold focuses on the scaffold's center, indicating that the central region plays a vital role in determining the strength. Whereas for the U2 scaffold, the attention is nearly uniformly distributed. Indeed, the FEM mechanical analysis confirmed this observation. Fig. 4(c) shows Von-Mises stress and hydrostatic pressure of B1 and U2 scaffolds, which analyzes the stress distribution and the strain behavior within the scaffold, respectively. The Von-Mises stress clearly illustrates that the B1 scaffold sacrifices the strength of the surrounding corner unit to promote the overall yield strength.

The hydrostatic pressure of the unit struts reveals that the more tensile deformation (positive orders) in the uniformly distributed structure implies a more bending deformation behavior. In contrast, the increase in the load-bearing capacity of the coarse middle unit of the B1 scaffold leads to a decrease in the tensile stress of the structure, creating a stretching-dominated structure, which contributes to its enhanced yield strength.

Table 1: Experimental result. A1(2) and B1(2) represent the best candidates from E500 tasks and E1000, respectively. U1(2) are the reference scaffold (uniform porosity) of E500 and E100.

Scaffolds Properties	A1	A2	U1	B1	B2	U2
Elastic modulus (MPa)	$494 \pm 15$	$520 \pm 28$	$508 \pm 53$	<b><math>1042 \pm 24</math></b>	$1012 \pm 22$	$975 \pm 19$
Yield Strength (MPa)	$12.5 \pm 1.2$	$12.3 \pm 0.7$	$13.5 \pm 0.3$	<b><math>27.0 \pm 0.8</math></b>	$21.8 \pm 0.7$	$21.7 \pm 1.8$
Porosity (%)	$55.5 \pm 1.1$	$55.8 \pm 1.5$	$54.8 \pm 1.6$	<b><math>35.4 \pm 1.1</math></b>	$37.6 \pm 0.9$	$38.3 \pm 1.2$

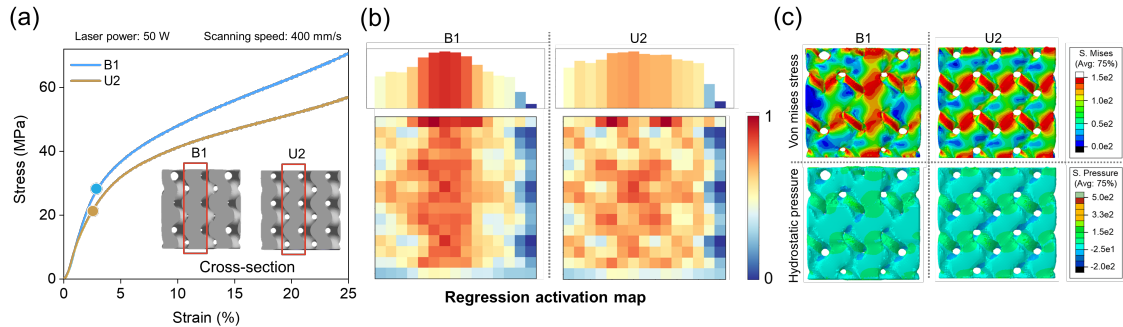


Figure 4: **Analysis of high yield strength cellular scaffold.** (a) Experimental compression curve of B1 and U2 scaffold. B1 outperforms U2 significantly. (b) Regression activation map normalized by the maximum value. (c) The Von-Mise stress (upper) and hydrostatic pressure analysis(lower).

## 2. Conclusion

We have proposed a data-efficient, multi-objective approach for designing complex cellular scaffolds with generative models and 3D neural networks. The approach quickly discovered Elastic-modulus-specific high-yield-strength cellular scaffolds with only 100 initial fine-tuned FEM simulation data. The final design was validated using the additive manufacturing technique. The TSG-MALL framework was proven to be a powerful tool that excels at constrained multi-objective optimization tasks in an infinite design landscape without any prior knowledge. Furthermore, the TSG-ALL framework provides interpretable patterns that bring new insights into the design philosophy of the cellular materials. Such new understanding provides a solid ground for further advanced multi-property optimization tasks of complex cellular materials. Therefore, by fusing high-precision simulation, machine learning, and additive manufacturing, our method opens a new pathway toward efficient multi-objective design of hierarchically structured materials.

## References

- Martín Abadi, Ashish Agarwal, Paul Barham, Eugene Brevdo, Zhifeng Chen, Craig Citro, Greg S. Corrado, Andy Davis, Jeffrey Dean, Matthieu Devin, Sanjay Ghemawat, Ian Goodfellow, Andrew Harp, Geoffrey Irving, Michael Isard, Yangqing Jia, Rafal Jozefowicz, Lukasz Kaiser, Manjunath Kudlur, Josh Levenberg, Dandelion Mané, Rajat Monga, Sherry Moore, Derek Murray, Chris Olah, Mike Schuster, Jonathon Shlens, Benoit Steiner, Ilya Sutskever, Kunal Talwar, Paul Tucker, Vincent Vanhoucke, Vijay Vasudevan, Fernanda Viégas, Oriol Vinyals, Pete Warden, Martin Wattenberg, Martin Wicke, Yuan Yu, and Xiaoqiang Zheng. TensorFlow: Large-scale machine learning on heterogeneous systems, 2015. URL <https://www.tensorflow.org/>. Software available from tensorflow.org.
- Laith Alzubaidi, Jinglan Zhang, Amjad J Humaidi, Ayad Al-Dujaili, Ye Duan, Omran Al-Shamma, J Santamaría, Mohammed A Fadhel, Muthana Al-Amidie, and Laith Farhan. Review of deep learning: concepts, CNN architectures, challenges, applications, future directions. *Journal of Big Data*, 8(1):53, 2021. ISSN 2196-1115. doi: 10.1186/s40537-021-00444-8. URL <https://doi.org/10.1186/s40537-021-00444-8>.
- Cécile M Bidan, Krishna P Kommareddy, Monika Rumpler, Philip Kollmannsberger, Peter Fratzl, and John W C Dunlop. Geometry as a factor for tissue growth: towards shape optimization of tissue engineering scaffolds. *Advanced healthcare materials*, 2(1):186–194, jan 2013. ISSN 2192-2640 (Print). doi: 10.1002/adhm.201200159.
- Johan Christensen, Muamer Kadic, Oliver Kraft, and Martin Wegener. Vibrant times for mechanical metamaterials. *MRS Communications*, 5(3):453–462, 2015. doi: 10.1557/mrc.2015.51.
- Shubhomoy Das, Weng-Keen Wong, Thomas Dietterich, Alan Fern, and Andrew Emmott. Incorporating expert feedback into active anomaly discovery. In *2016 IEEE 16th International Conference on Data Mining (ICDM)*, pages 853–858, 2016. doi: 10.1109/ICDM.2016.0102.
- David Downing, Alistair Jones, Milan Brandt, and Martin Leary. Increased efficiency gyroid structures by tailored material distribution. *Materials & Design*, 197:109096, 2021. ISSN 0264-1275. doi: <https://doi.org/10.1016/j.matdes.2020.109096>. URL <https://www.sciencedirect.com/science/article/pii/S0264127520306316>.
- Paul Z. Hanakata, Ekin D. Cubuk, David K. Campbell, and Harold S. Park. Accelerated Search and Design of Stretchable Graphene Kirigami Using Machine Learning. *Physical Review Letters*, 121(25):255304, 2018. ISSN 10797114. doi: 10.1103/PhysRevLett.121.255304. URL <https://doi.org/10.1103/PhysRevLett.121.255304>.
- Dongchan Jang, Lucas R Meza, Frank Greer, and Julia R Greer. Fabrication and deformation of three-dimensional hollow ceramic nanostructures. *Nature Materials*, 12(10):893–898, 2013. ISSN 1476-4660. doi: 10.1038/nmat3738. URL <https://doi.org/10.1038/nmat3738>.
- Muamer Kadic, Tiemo Bückmann, Nicolas Stenger, Michael Thiel, and Martin Wegener. On the practicability of pentamode mechanical metamaterials. *Applied Physics Letters*, 100(19):191901, 2012. doi: 10.1063/1.4709436. URL <https://doi.org/10.1063/1.4709436>.

- Alex Krizhevsky, Ilya Sutskever, and Geoffrey E. Hinton. Imagenet classification with deep convolutional neural networks. *Commun. ACM*, 60(6):84–90, may 2017. ISSN 0001-0782. doi: 10.1145/3065386. URL <https://doi.org/10.1145/3065386>.
- Jensen Li, Lee Fok, Xiaobo Yin, Guy Bartal, and Xiang Zhang. Experimental demonstration of an acoustic magnifying hyperlens. *Nature Materials*, 8(12):931–934, 2009. ISSN 1476-4660. doi: 10.1038/nmat2561. URL <https://doi.org/10.1038/nmat2561>.
- Xiaoyan Li and Huajian Gao. Smaller and stronger. *Nature Materials*, 15(4):373–374, 2016. ISSN 1476-4660. doi: 10.1038/nmat4591. URL <https://doi.org/10.1038/nmat4591>.
- F Magnus, B Wood, J Moore, K Morrison, G Perkins, J Fyson, M C K Wiltshire, D Caplin, L F Cohen, and J B Pendry. A d.c. magnetic metamaterial. *Nature Materials*, 7(4):295–297, 2008. ISSN 1476-4660. doi: 10.1038/nmat2126. URL <https://doi.org/10.1038/nmat2126>.
- Yunwei Mao, Qi He, and Xuanhe Zhao. Designing complex architected materials with generative adversarial networks. *Science Advances*, 6(17), 2020. ISSN 23752548. doi: 10.1126/sciadv.aaz4169.
- Ole Sigmund Martin P. B. *Topology Optimization: Theory, Methods, and Applications*. Springer, 2003.
- Fanman Meng, Kaixu Huang, Hongliang Li, and Qingbo Wu. Class activation map generation by representative class selection and multi-layer feature fusion, 2019. URL <https://arxiv.org/abs/1901.07683>.
- Lucas R. Meza, Satyajit Das, and Julia R. Greer. Strong, lightweight, and recoverable three-dimensional ceramic nanolattices. *Science*, 345(6202):1322–1326, 2014. doi: 10.1126/science.1255908. URL <https://www.science.org/doi/abs/10.1126/science.1255908>.
- Yu Qin, Aobo Liu, Hui Guo, Yunong Shen, Peng Wen, Hong Lin, DanDan Xia, Maximilian Voshage, Yun Tian, and Yufeng Zheng. Additive manufacturing of zn-mg alloy porous scaffolds with enhanced osseointegration: In vitro and in vivo studies. *Acta Biomaterialia*, 2022a. ISSN 1742-7061. doi: <https://doi.org/10.1016/j.actbio.2022.03.055>. URL <https://www.sciencedirect.com/science/article/pii/S1742706122001945>.
- Yu Qin, Hongtao Yang, Aobo Liu, Jiabao Dai, Peng Wen, Yufeng Zheng, Yun Tian, Shuang Li, and Xiaogang Wang. Processing optimization, mechanical properties, corrosion behavior and cytocompatibility of additively manufactured zn-0.7li biodegradable metals. *Acta Biomaterialia*, 142:388–401, 2022b. ISSN 1742-7061. doi: <https://doi.org/10.1016/j.actbio.2022.01.049>. URL <https://www.sciencedirect.com/science/article/pii/S1742706122000599>.
- Ziyuan Rao, PoYen Tung, Ruiwen Xie, Ye Wei, Hongbin Zhang, Alberto Ferrari, T. P. C. Klaver, Fritz Körmann, Prithiv Thoudden Sukumar, Alisson Kwiatkowski da Silva, Yao Chen, Zhiming Li, Dirk Ponge, Jörg Neugebauer, Oliver Gutfleisch, Stefan Bauer, and Dierk Raabe. Machine learning-enabled high-entropy alloy discovery, 2022. URL <https://arxiv.org/abs/2202.13753>.

Neil Rubens, Mehdi Elahi, Masashi Sugiyama, and Dain Kaplan. *Active Learning in Recommender Systems*, pages 809–846. Springer US, Boston, MA, 2015. ISBN 978-1-4899-7637-6. doi: 10.1007/978-1-4899-7637-6\_24. URL [https://doi.org/10.1007/978-1-4899-7637-6\\_24](https://doi.org/10.1007/978-1-4899-7637-6_24).

Stuart J Russell and Peter Norvig. *Artificial intelligence: a modern approach*. Malaysia; Pearson Education Limited,, 2016.

T. A. Schaedler, A. J. Jacobsen, A. Torrents, A. E. Sorensen, J. Lian, J. R. Greer, L. Valdevit, and W. B. Carter. Ultralight metallic microlattices. *Science*, 334(6058):962–965, 2011. doi: 10.1126/science.1211649. URL <https://www.science.org/doi/abs/10.1126/science.1211649>.

D. Schurig, J. J. Mock, B. J. Justice, S. A. Cummer, J. B. Pendry, A. F. Starr, and D. R. Smith. Metamaterial electromagnetic cloak at microwave frequencies. *Science*, 314(5801):977–980, 2006. doi: 10.1126/science.1133628. URL <https://www.science.org/doi/abs/10.1126/science.1133628>.

Michael Smith. *ABAQUS/Standard User’s Manual, Version 6.9*. Dassault Systèmes Simulia Corp, United States, 2009.

Lorenzo Valdevit, Alan J. Jacobsen, Julia R. Greer, and William B. Carter. Protocols for the optimal design of multi-functional cellular structures: From hypersonics to micro-architected materials. *Journal of the American Ceramic Society*, 94(s1):s15–s34, 2011. doi: <https://doi.org/10.1111/j.1551-2916.2011.04599.x>. URL <https://ceramics.onlinelibrary.wiley.com/doi/abs/10.1111/j.1551-2916.2011.04599.x>.

Pai Wang, Filippo Casadei, Sicong Shan, James C. Weaver, and Katia Bertoldi. Harnessing buckling to design tunable locally resonant acoustic metamaterials. *Phys. Rev. Lett.*, 113:014301, Jul 2014. doi: 10.1103/PhysRevLett.113.014301. URL <https://link.aps.org/doi/10.1103/PhysRevLett.113.014301>.

Xiaojian Wang, Shانqin Xu, Shiwei Zhou, Wei Xu, Martin Leary, Peter Choong, M. Qian, Milan Brandt, and Yi Min Xie. Topological design and additive manufacturing of porous metals for bone scaffolds and orthopaedic implants: A review. *Biomaterials*, 83:127–141, 2016. ISSN 0142-9612. doi: <https://doi.org/10.1016/j.biomaterials.2016.01.012>. URL <https://www.sciencedirect.com/science/article/pii/S0142961216000144>.

Hongtao Yang, Bo Jia, Zechuan Zhang, Xinhua Qu, Guannan Li, Wenjiao Lin, Donghui Zhu, Kerong Dai, and Yufeng Zheng. Alloying design of biodegradable zinc as promising bone implants for load-bearing applications. *Nature Communications*, 11(1):401, 2020. ISSN 2041-1723. doi: 10.1038/s41467-019-14153-7. URL <https://doi.org/10.1038/s41467-019-14153-7>.

Ting Yang, Hongshun Chen, Zian Jia, Zhifei Deng, Liuni Chen, Emily M. Peterman, James C. Weaver, and Ling Li. A damage-tolerant, dual-scale, single-crystalline microlattice in the knobby starfish, *< i> protoreaster nodosus </i>*. *Science*, 375(6581):647–652, 2022. doi: 10.1126/science.abj9472. URL <https://www.science.org/doi/abs/10.1126/science.abj9472>.

Xiaoyu Zheng, Howon Lee, Todd H. Weisgraber, Maxim Shusteff, Joshua DeOtte, Eric B. Duoss, Joshua D. Kuntz, Monika M. Biener, Qi Ge, Julie A. Jackson, Sergei O. Kucheyev, Nicholas X. Fang, and Christopher M. Spadaccini. Ultralight, ultrastiff mechanical metamaterials. *Science*, 344(6190):1373–1377, 2014. doi: 10.1126/science.1252291. URL <https://www.science.org/doi/abs/10.1126/science.1252291>.

## Acknowledgments

This work was supported by the National Key R&D Program of China (grant number 2018YFE0104200) and the National Natural Science Foundation of China (grant number 52175274, 51875310); Ye Wei would like to acknowledge financial support of Shuimu fellowship program from Tsinghua University.

## Appendix

### Additive manufacturing

We used a laser powder bed fusion machine (manufacturer: Xi'an Bright Laser Technologies Co., Ltd, model: BLT-S210) to produce specimens with pure Zinc powder. The Zinc samples were additively manufactured with a laser power of 40W, a laser scanning speed of 500mm/s, and a layer thickness of 0.03mm. In an argon atmosphere where oxygen content was under 0.01%, the Zinc specimens reached high printing quality (relative density over 99%). we fabricate the ML-predicted scaffold and its uniform-designed counterpart. These two structures possessed the same mean porosity and were to be tested and compared in the following compression test. The as-built scaffolds were compressed using a universal testing machine (Shimadzu AG-X100KN) according to ASTM E9-2009 at room temperature ( 20°C). The strain rate was set constant of 0.05/min.

### Data generation

The unlabeled dataset consisting of 21 000 data points was generated for the training of the 3D-CAE. As the porosity can take any value from 0 to 1, the possible arrangement is infinite. To simplify the problem, we only allow the scaffold's porosity takes fixed values (0.2 to 0.8, interval 0.1) to reduce the design space. Nevertheless, there are still  $7^{27}$  possible combinations. 3000 different porosity matrices were generated at each interval. For each interval, there are three kinds of symmetry in the database (Fig. 5(a)): central, vertical, horizontal and one random arrangement. The porosity matrix also have three kinds (Fig. 5(b)):  $2 * 2 * 2, 3 * 3 * 3$  and  $4 * 4 * 4$ , which then all expand to a  $12 * 12 * 12$  matrix. In such a way, our 3D-CAE can generate three different kinds of porosity matrices. In this study, the  $3 * 3 * 3$  was chosen to balance structural complexity and computational efficiency. But in principle, our TSG-ALL can handle three different kinds of scaffold arrangements.

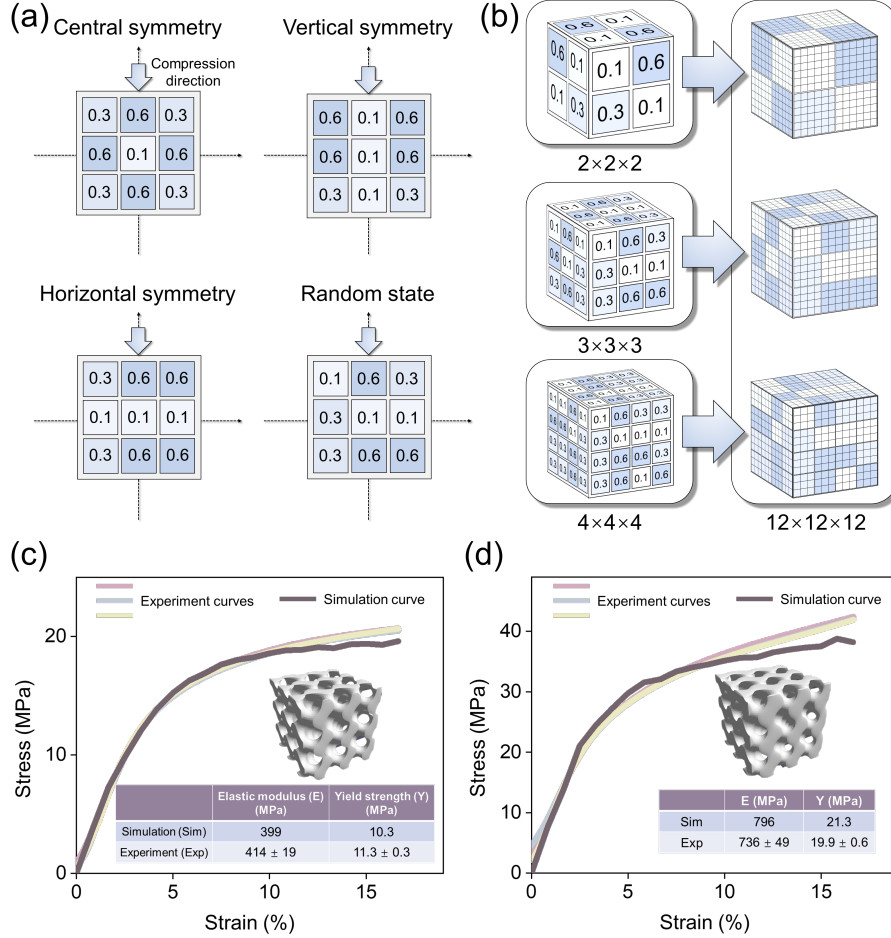


Figure 5: **(a, b, c, d)** Data generation and simulation calibration. (a, b) The porosity matrix database contains three symmetry and one random arrangement. there are 3 kinds of porosity matrix types. (c, d) The FEM simulation agrees with experimental observations. Experimental and numerical results of a random scaffold with mean porosity of 0.55 and 0.42.

One hundred scaffolds were uniformly sampled from the unlabeled database and their corresponding E and Y were computed by FEM. The FEM accuracy is guaranteed through careful calibration with experimental data. Fig. 5 (c, d) shows the simulation and experimental data of two randomly selected scaffolds. It was confirmed that the deviations between experiment and simulation are less than 10%. ABAQUS/Explicit software was used for compression simulations(Smith, 2009).

### Numerical simulation parameters

The finite element method was based on the same rigid-cylinder and deformable-implant-structure model. The material was homogeneous, and the Poisson's ratio was 0.25. The modulus of elasticity was set to 5 GPa and the yield strength to 120 MPa based on the compression experiments of the block pure Zn prepared by LPBF. Ductile damage was used to simulate the plastic deformation to

the failure stage. Fracture strain was set as 0.03, and the effects of triaxiality deviation and strain rate were neglected. We extracted displacements and forces in post-processing and then converted them to strains and stresses, respectively.

### Machine learning algorithms

The 3D-CAE consists of an encoder and decoder. The encoder is composed of 3 3D convolutional layers (Conv3D). The input size is (12,12,12,1). The first, second, third, and fourth layers contain 60, 30, and 15 filters. There are three max-pooling layers between the convolutional layers, responsible for the down-sampling. For example, one max pooling layer will reduce the size of Conv3D from (12,12,12) to (6,6,6), shrink each (2,2,2) box down to (1,1,1) and taking the maximum as its value. The size of the final layer is (3,3,3,15). Another max-pooling reduces it to the hidden representation (1,1,1,x), where x represents the dimension. The decoder is of the same Con3D architecture, but this time with up-sampling, converting the hidden feature (1,1,1,x) back to (12,12,12,1). Reconstruction loss is the mean square error between input and output. Fig. 6 (a) shows the training history of 3D-CAE with eight latent dimensions. The loss quickly drops to near zero after 60 epochs. The histogram (inlet) shows that the 4-dimension error is too high, and sampling from the 16-dimension is too time-consuming. It was evidenced that 8-dimension reaches a balance between loss and efficiency.

The 3D-CNN architecture consists of 3 convolutional layers. The first, second and third layers contain 8, 4 and 2 filters, respectively; three max-pooling layers are located behind each convolutional layer. Finally, before reaching the output node, the last layer was flattened into 1048 neurons, followed by a series of fully connected layers (128, 64, 32). The activation function is the exponential linear unit. And the loss function is the mean square error. The program was written using Keras and Tensorflow (Abadi et al., 2015).

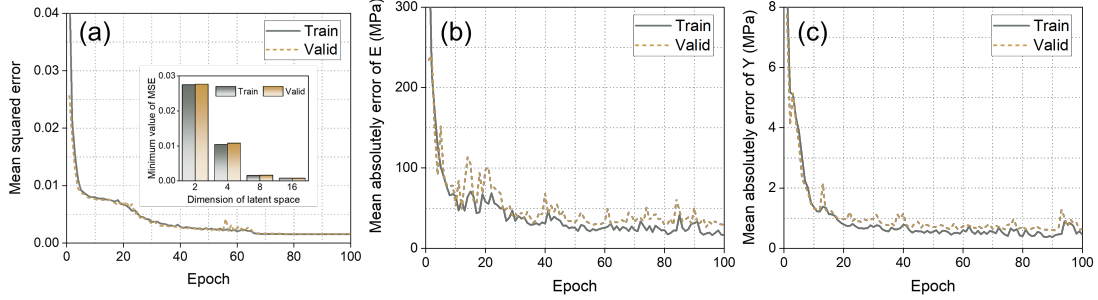


Figure 6: (a) 3D-CAE training history. (b and c) The training history of 3D-CNNs for Elastic modulus and Yield's Strength prediction.

Table 2: Mean and standard deviation of elastic modulus and yield strength at each iteration of TSG MALL.

	E500 Task			E1000 Task		
	Elastic modulus (MPa)	Yield strength (MPa)	Porosity (%)	Elastic modulus (MPa)	Yield strength (MPa)	Porosity (%)
Iteration	1	$546 \pm 52$	$12.9 \pm 0.8$	$55.4 \pm 0.5$	$1027 \pm 22$	$26.2 \pm 0.7$
	2	$508 \pm 19$	$12.1 \pm 0.6$	$56.6 \pm 0.8$	$1297 \pm 85$	$32.1 \pm 1.3$
	3	$568 \pm 34$	$15.2 \pm 0.9$	$54.2 \pm 0.9$	$1105 \pm 68$	$28.8 \pm 0.8$
	4	$559 \pm 30$	$14.8 \pm 0.8$	$53.5 \pm 1.1$	$980 \pm 24$	$29.1 \pm 0.5$
	5	$515 \pm 16$	$14.2 \pm 0.7$	$56.4 \pm 0.2$	None	None